frontiers | Frontiers in Photobiology

TYPE Original Research
PUBLISHED 13 January 2025
DOI 10.3389/fphbi.2024.1452747

OPEN ACCESS

EDITED BY
Herwig Stibor,
Ludwig Maximilian University of Munich, Germany

REVIEWED BY
Rose Cory,
University of Michigan, United States
Paul Bukaveckas,
Virginia Commonwealth University, United States

*CORRESPONDENCE
Aleksandr Berezovski,
aleksandrberezovski@gmail.com

RECEIVED 21 June 2024
ACCEPTED 20 December 2024
PUBLISHED 13 January 2025

CITATION
Berezovski A, Hessen DO and Andersen T (2025) Photon budgets and the relative effects of CDOM and pigment absorptions on primary production along a coastal salinity gradient. *Front. Photobiol.* 2:1452747. doi: 10.3389/fphbi.2024.1452747

Photon budgets and the relative effects of CDOM and pigment absorptions on primary production along a coastal salinity gradient

Aleksandr Berezovski*, Dag O. Hessen and Tom Andersen

Department of Biosciences, Centre for Biogeochemistry in the Anthropocene, University of Oslo, Oslo, Norway

The study highlights the critical role of CDOM in coastal light attenuation and its impact on primary production (PP). We investigated the spectral attenuation of light due to water, phytoplankton pigments, detritus and coloured dissolved organic matter (CDOM) along a salinity gradient in the outer Oslofjord, Norway. By examining the effects of these components across different seasons, we aimed to elucidate their relative contributions to light absorption and PP. The findings suggest that increased terrestrial CDOM inputs, driven by climate, changed atmospheric deposition and land-use changes, could significantly affect coastal ecosystems by altering light attenuation and consequently PP and potentially leading to other ecological pressures. CDOM consistently dominated light absorption across all stations and seasons, contributing 50%–80% of the total absorption of photosynthetically active radiation. The absorption by CDOM and detritus decreased with increasing salinity, while phytoplankton absorption followed a seasonal succession. PP estimates show high seasonal variability from maximums in June to minimums in November, mainly attributed to, changes in seasonal light availability and phytoplankton biomass, followed by light attenuation by CDOM and differences in quantum yields of photosystem II (PSII). Nutrient analysis showed a seasonal pattern, with the highest nitrogen concentrations in November and depletion during more productive seasons, as well as conservative mixing throughout the salinity gradient. CDOM absorption played substantial, albeit not leading, role in influencing PP estimates, derived from a bio-optical model. CDOM was the main determinant of light attenuation across most wavelegnths.

KEYWORDS

dissolved organic carbon, light attenuation, spectral absorbance, absorption coefficients, primary production, photosynthesis

1 Introduction

Coloured substances in the water column, including water itself, determine light attenuation. Other major light-absorbing components, besides water, are phytoplankton, organic or inorganic particles, as well as dissolved organic matter (DOM). The contribution of these compounds varies among systems and across different parts of the spectrum, but notably coloured dissolved organic matter (CDOM) of terrestrial origin is strongly chromophoric, impacting downwelling photosynthetically active radiation, primarily at

shorter wavelengths (Thrane et al., 2014). The molecular size and structure of CDOM may affect its light-absorbing properties, and also iron (Fe), typically associated with allochthonous DOM may add to light attenuation (Kritzberg and Ekström, 2012; Xiao et al., 2013; Weyhenmeyer et al., 2014).

During the past decades, a pronounced increase in CDOM ("browning") have been observed in boreal freshwaters with subsequent impact also on coastal and marine systems (Creed et al., 2018; Wit et al., 2021; Dupont and Aksnes, 2013). This browning has multiple causes related to climate change: reduced acidification (Monteith et al., 2007), increased forest mass and production (Finstad et al., 2016), increased precipitation and runoff (de Wit et al., 2016); as well as direct anthropogenic causes, such as changes in land use, agricultural and forestry practices and "channelling" of rivers and streams (Kritzberg, 2017; Opdal et al., 2024). Also increased CO_2 directly promoting terrestrial C-fixation or indirectly by warming translate into more vegetation notably in the northern ecosystems that are disproportionately affected by climate change (Hansen et al., 2006; Wang et al., 2023). The accumulating plant biomass on land leads to higher rates of organic matter export to aquatic systems (Larsen et al., 2011). As this CDOM enters coastal waters, some is lost by flocculation and the most labile fractions may be lost by oxidation, but the major fraction appears quite recalcitrant to biodegradation, as it partly consists of lignin (Opsahl and Benner, 1997; Nebbioso and Piccolo, 2013), and have caused pronounced "coastal darkening" in northern coastal areas (Opdal et al., 2019; Opdal et al., 2023). When light hits the water surface, some of the light is reflected, while the rest is absorbed by water and coloured compounds. With more turbid waters and an increasing riverine flux of coloured, terrestrially derived CDOM to coastal waters, there will be less light penetrating into the deeper water layers (Opdal et al., 2019). Coastal darkening effects can be especially pronounced in fjords, as they have deep basins, and the cumulative effects of darkening increase with depth. Also the fjords are located on the shoreline, and therefore closer to the sources of CDOM compared to open deep seas (Aksnes et al., 2004; Aksnes et al., 2009).

Darkening has widespread ecosystem consequences; most importantly, the reduced availability of photons in the photosynthetically active radiation (PAR) range will affect photosynthetic depth and reduce both pelagic and benthic primary production (Thrane et al., 2014; Blain et al., 2021). As a consequence, it will also affect vertical gas profiles, increasing the likelihood of deep-water anoxia and affect the overall gas balance (increased CO_2:O_2; Allesson et al., 2022). It may also have temporal impacts on phytoplankton by affecting the onset of the spring bloom as observed in the North Sea (Opdal et al., 2019), or lead to phytoplankton community changes (Lyche Solheim et al., 2024). Thus, CDOM enrichment could lead to shallowing of critical depth (Sverdrup, 1953), which in turn leads to seasonal delays of phytoplankton bloom (Diehl et al., 2015). Alterations of phytoplankton blooms can cause mismatches with zooplankton and fish spawning seasons. This potentially leads to food scarcity for fish, which, in turn, could result in recruitment failure (Johannessen et al., 2012; Opdal et al., 2024). These cascading effects can impact entire ecosystems and pose socio-economic risks related to negative impacts on commercial fish stocks. Since most of CDOM is of terrestrial origin, the darkening effect should be the most pronounced in the near-coastal areas, where it may have substantial impacts on the ecosystems not only by affecting the phytoplankton communities, but also changing the compensation depth for kelp and other macroalgae. For example, kelp forests along the Swedish Skagerrak coast have been observed to succumb to fast-growing macroalgae and phytoplankton due to limited light availability and other synergistic effects (Frigstad et al., 2013; Eriksson et al., 2002). Darkening also directly affects visual feeders like most fish species (Blain et al., 2021; Eiane et al., 1997). Aksnes et al. (2004) demonstrated that fjords with higher light attenuation had lower fish biomass and increased zooplankton size. This was attributed to murkier waters being a disadvantage for fish that depend on vision for predation, which in turn allowed zooplankton to grow larger in size. Aksnes et al. (2009) further argue that coastal darkening could even lead to regime shifts in deep fjords, i.e., jellyfish (tactile predator) gaining a competitive edge over fish (visual predator).

In this study we aimed to quantify the contribution of four major components to total light attenuation (water, phytoplankton pigments, non-algal particles and CDOM) in the PAR range. This was done for various seasons along a transect in the Oslofjord, Norway, from the high CDOM inner estuary at the mouth of Glomma, Norway's largest river, to the low-CDOM open, oceanic waters. The transect represented a natural salinity gradient with decreasing riverine impact. Secondly, we aimed to estimate on how this might affect primary production. This was done by using a bio-optical model based on the fraction of photons trapped by phytoplankton pigments (Suggett et al., 2010; Thrane et al., 2014) along the same gradient. This allows for predictions of spatial and temporal change in pelagic primary production related to optical properties and CDOM-related darkening.

2 Materials and methods

2.1 Study site and sampling methods

Six stations in the outer Oslofjord were visited on six separate cruises (Figure 1). These stations are selected to represent a salinity gradient with gradual mixing of riverine water with oceanic water from L1 to OF2 (Table 1), where the prevalence of terrestrially derived DOM was expected to be negatively correlated with the salinity. The inner station represents the outlet of river Glomma, the largest river of Norway draining 40,464 km^2 of boreal uplands (NVE Sildre, 2024) and contributing over 40% of total freshwater supply to the Hvaler basin (Walday et al., 2023). Water samples were collected at each station from 3–4 m depths and were kept at 2°C until analyses. The 3–4 m depth represents mixed layer, however the top of mixed layer at the more marine stations at times was deeper (7–10 m). Riverine station stratification is highly dynamic, depending on precipitation, and can vary from 5–15 m. The area is undergoing typical fjord mixing, with brackish freshwater on the top moving out to outer fjord and salty water entering the estuary on the bottom (Sætre, 2007). The sampling dates (04.06.2020, 08.09.2020, 26.11.2020, 23.02.2021, 25.03.2021 and 17.06.2021) encompassed different seasons to study the intra-annual changes in water chemistry and flood events in the area and the implications for phases of phytoplankton succession.

10.3389/fphbi.2024.1452747

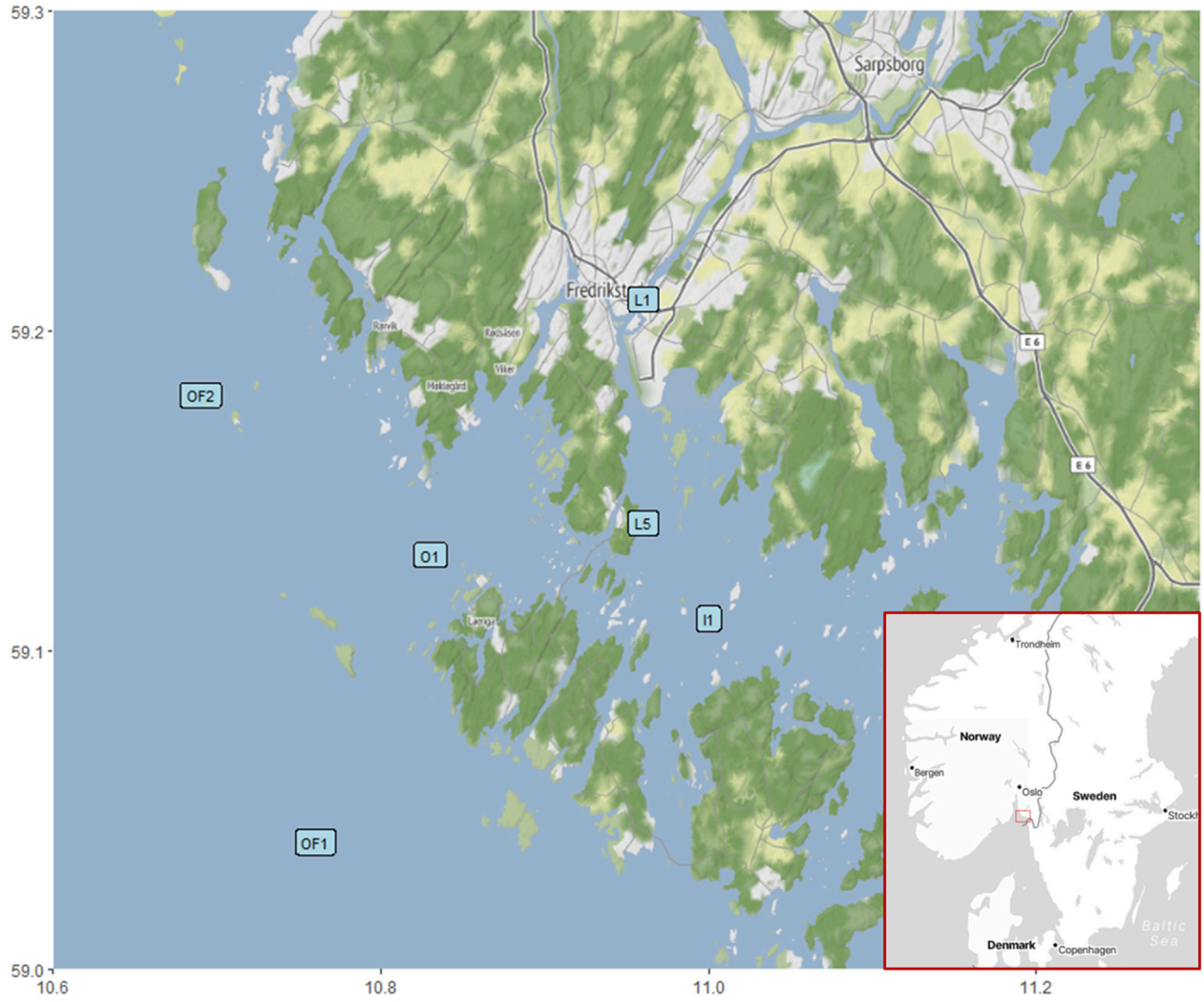

FIGURE 1
Sampling area encompassing six stations and the location of the area on a map of Scandinavia (bottom right corner).

TABLE 1 Details of the sampling stations.

Station code	Location name	Latitude (N)	Longitude (E)	Water depth (m)	Distance to Glomma (km)	Mixed layer depth (m)	Bottom water T (°C)	S at 3 m (PSU)
L1	Glomma	59.211550	10.961717	22	0	7	6.5	1.8
L5	Kjøkøy	59.146500	10.960933	52	7.6	5	6.6	18.7
I1	Ramsø	59.109333	11.002717	50	12.4	6	6.6	16.9
O1	Leira	59.136517	10.833617	50	20.4	7	11	20.3
OF1	Torbjørnskjær	59.040117	10.760550	452	30.4	10	7	23.7
OF2	Missingene	59.185950	10.691683	352	31.9	8	6.4	24.5

Stratification depth, T (temperature) and S (salinity) are averaged between the sampling dates.

As the area is strongly influenced by the freshwater from Glomma (average daily discharge of 684 m^3 s^{-1}; NVE Sildre, 2024), the salinities fluctuate heavily over the year. After periods of snowmelt or heavy precipitation, water masses transport large amounts of CDOM to the fjord, while dry periods are characterized by higher salinities and less CDOM. Two June samplings were included to capture the peak of summer flood periods in two different years (Supplementary Figure 1). March and September

cruises were designated to represent the start and the end of the summer flood respectively, while November and February were the start and the end of the low productivity winter season. Typical phytoplankton bloom phenology in the area is characterized by a spring bloom in March, summer bloom in June and autumn bloom in September (Lundsør et al., 2020).

2.2 Bio-optical measurements

Spectral absorption of particulate matter was measured using a filter pad method (Roesler et al., 2018) in a integrating sphere (ISR 2200, Shimadzu scientific instruments, Columbia, Maryland, United States) connected to a Shimadzu UV-2550 UV-VIS spectrophotometer. The method allowed to measure two types of particulate matter–phytoplankton (pigments) and non-algal particles absorbance (NAP). NAP includes both organic and inorganic particles and is hereafter referred to as detritus. Pigment and detritus absorbances could then be compared to the other two absorbance constituents considered in the study—CDOM and water. The integrating sphere allowed to measure the absorbance of the materials which had large scattering properties (i.e., the filter and the particles on it). The procedure followed (Thrane et al., 2014), utilising (Bricaud and Stramski, 1990)'s path length amplification correction. In brief, 500 mL of sample water was filtered through a GF/F glass fiber filter (0.7 µm pore size), after which the filter, along with a blank filter soaked with MilliQ water, were placed inside the integrating sphere for absorbance measurement (Röttgers and Gehnke, 2012). This ensured that nearly all photons scattered by the sample were detected and that the absorbance of the blank filter was automatically subtracted from that of the sample filter, improving accuracy and precision of absorption measurements (Roesler et al., 2018). The filtration occurred on the next day after sampling (water samples were kept at 4°C), while the absorbance measurements happened on the day after this (filters were kept at −20°C). The filters were thawed and hydrated before the analysis. The measured absorbance was limited to PAR region (400–700 nm; Kirk, 1994). After the initial measurement of absorbance by all particles retained on the filter, the filter was bleached with 200 µL sodium hypochlorite according to the method of Tassan and Ferrari (1995). After the filter was bleached for 2 min, removing all the pigments, the absorbance was measured once again to get detritus (not being bleached) absorbance (A_d). The A_d spectrum was subtracted from the total absorbance spectrum, resulting in *in vivo* pigment absorbance spectrum (A_p). A_p included all absorbances by various pigments collected on the filter. A_d and A_p were corrected for scattering and "instrument drift" (Nelson and Guarda, 1995) - by subtracting average absorbance between 740 and 750 nm from the absorbance at each wavelength.

Base e absorption coefficients are traditionally used in bio-optical calculations due to mathematical convenience, since they do not introduce a scaling factor in differentiation and integration. Therefore, the pigment absorption coefficients [a_p (λ)] were then calculated by transforming base 10 absorbance units (A_p) into base e units and dividing it by dimensions of a cylinder representing the volume of filtered water (V, m^3) and the area of used GF/F filter (A, m^2) to get m^{-1} units (Equation 1).

$$a_p(\lambda) = \frac{A_p - A_d}{\frac{V}{A}} * \ln(10) \quad (1)$$

The detritus coefficients were calculated similarly, but solely from the bleached samples (Equation 2).

$$a_d(\lambda) = \frac{A_d}{\frac{V}{A}} * \ln(10) \quad (2)$$

The filtrate was used for CDOM absorbance measurements. CDOM absorbance was measured on the same spectrophotometer, but without the integrating sphere. Two 5 cm (L = 0.05 m) quartz cuvettes were placed into the spectrophotometer, one containing MilliQ water as a baseline reference and the other containing the sample. The measurement resulted in CDOM absorbance (A_{CDOM}). A_{CDOM} was corrected for scattering using an average absorbance between 650 and 750 nm, as CDOM absorbs miniscule amount of light in this waveband. The absorbance units were transformed into absorption coefficients [a_{CDOM} (λ)] as in Equation 3.

$$a_{CDOM}(\lambda) = \ln(10) * \frac{A_{CDOM}}{L} \quad (3)$$

Having three different absorption coefficients, as well as constant water absorption coefficients (a_{H2O}; Morel and Prieur, 1977), allows for adding all four together to get an absorption sum, and consecutively finding fraction absorbed by photosynthetic pigments [$Fp(\lambda)$; Equation 4]. Detritus [$F_d(\lambda)$], CDOM [$F_{CDOM}(\lambda)$] and water [$F_{H2O}(\lambda)$] absorption fractions were calculated in the same manner. Averaging absorption fraction over PAR range would result in PAR-averaged fractions of absorption by the four components ($\overline{F_p}$, $\overline{F_d}$, $\overline{F_{CDOM}}$ and $\overline{F_{H2O}}$).

$$F_p(\lambda) = \frac{a_p(\lambda)}{\left(a_p(\lambda) + a_d(\lambda) + a_{CDOM}(\lambda) + a_{H2O}(\lambda)\right)} \quad (4)$$

About 500 mL of water samples were filtered through syringe filters for chlorophyll *a* (chl*a*) concentrations analysis (0.22 µm pore size, Sterivex™). The filters were then frozen in −40°C until the day of analysis. Once the filters were thawed, they were filled with 2 mL of ethanol (90%) to extract chl*a* that was collected on filters. We subsampled ethanol extracts into a well plate (200 µL) and measured chlorophyll fluorescence on a microplate reader (Synergy™ MX, BioTek, Winooski, Vermont, United States), calibrated with a commercial chlorophyll *a* standard (Sigma-Aldrich C5753). chl*a* concentrations were transformed to µg/L by dividing the concentration measured with the plate reader (µg/mL) by volume of sample water (L) and multiplied by the ethanol volume used to extract the pigments from the filter (2 mL).

Pulse amplitude modulated fluorometry (Schreiber, 2004) allows to estimate quantum yield of photosystem II (QY), which is defined as the number of photons used for photochemistry relative to the total number of photons absorbed by pigment (Raval et al., 2023). This is effectively a measure of the utilization of absorbed photons by the photosynthetic pigments in living cells. The closer QY of a photosynthetic pigment is to 0.8 (theoretical maximum QY), the more efficiently the cells use captured light in photosynthetic pathways. After exposing the water samples to darkness for an hour, QY was measured as a function of light intensity [QY(E)] using AquaPen-C's (AP-C 100, Photon Systems Instruments, Czech Republic) "light curve 1" protocol with blue

light excitation at 450 nm. Based on Cullen and Davis (2003) we tried to run distilled water blanks with Aquapen, but since the resulting QY light curves were very noisy and uninformative, our best blank estimate is close to zero with a large standard error.

2.3 Primary production estimation

Bio-optical primary production estimation (e.g., Smith et al., 1989) involves combining the photon capture rate by photosynthetic pigments with quantum efficiency of photosynthesis on a given depth and time. Integrating this quantity over depth and time gives the daily, area specific bio-optical production rate which can be converted to an estimate of daily, area specific carbon fixation (mg C m^{-2} day^{-1}).

We extracted time series of hourly surface PAR irradiance averages from the STRÅNG database (STRÅNG, 2024) for each station's coordinates and each sampling date. Using a conversion factor from Thimijan and Heins (1983), we converted the daily PAR irradiance time series $E_0(t)$ from the original energy units (W m^{-2}) to quantum flux (mol quanta m^{-2} day^{-1}). For consistency with Thrane et al. (2014) we used absorption coefficients averaged across the PAR range instead of integrating wavelength-specific rates. In Supplementary Figure 2 we show that this approximation gives very similar results to a fully spectrally resolved bio-optical model. So, assuming we can represent the PAR-averaged (400–700 nm) vertical light attenuation coefficient $\bar{k}$ as the sum of all PAR-averaged light absorption components ($\bar{k} = \overline{a_p} + \overline{a_d} + \overline{a_{CDOM}} + \overline{a_{H2O}}$), we could compute the local PAR irradiance at a given depth (z; m) and time of day (t; fractional day) from Equation 5.

$$E_{(z,t)} = E_0(t)e^{-\bar{k}z} \tag{5}$$

The local, volumetric PAR absorption rate [$\Delta E(z,t)$; mol quanta m^{-3} day^{-1}] is the difference between irradiance at the top and the bottom of a layer, divided by the depth of that layer (Δz; m). We have measured the irradiance at surface water and 10 m depth using hyperspectral irradiance sensor (RAMSES, TriOS GmbH, Rastede, Germany) coupled with another sensor installed on deck for reference (atmospheric irradiance) measurements. This ensured that the majority of photosynthetic activity was captured and that the stratification depth was reached in the majority of cases (excluding only riverine station during the highest discharge seasons). $\Delta E(z,t)$ is, therefore, calculated using Equation 6.

$$\Delta E(z,t) = \frac{E(z,t) - E(z+\Delta z,t)}{\Delta_z} = \frac{E(z,t)}{\Delta_z}\left(1 - e^{-\bar{k}\Delta z}\right) \tag{6}$$

Local C fixation rate ($PP(z,t)$; mol C m^{-3} day^{-1}; Equation 7) is the product of PAR absorption rate ($\Delta E(z,t)$ times fraction absorbed by photosynthetic pigments [$Fp(\lambda)$], adjusted for the quantum efficiency at local irradiance {$QY[E(z,t)]$}, and converted by the C fixation yield per quanta absorbed (QC = 12 mol quanta/mol CO_2; Kirk, 1994).

$$PP(z,t) = \Delta E(z,t) \cdot QY(E(z,t)) \cdot F_p(\lambda) \cdot QC^{-1} \tag{7}$$

We parameterized the light response of quantum yield, $QY(E)$, as a log-linear function based on light curve assays with the Aquapen instrument. This implicitly assumes that the quantum yield of photosystem I has the same light response as photosystem II (which the Aquapen measures).

We finally estimated daily primary production (PP) by integrating Equation 7 over depth and time, and converting the result from mol CO_2 m^{-2} day^{-1} to mg C m^{-2} day^{-1}. For illustration, we show the depth and time distributions of the outputs of Equations 5–7 for a particular date and station (station L5 on 15.06.2021) in Figure 2. Panels 2A, C and E represent, $E(z,t)$, $QY(z,t)$ and $PP(z,t)$ in the upper 5 m of water column throughout the day. Right column (panels 2B, D and F) shows the surface PAR irradiance time-series $E_0(t)$ as well as the integrals of $PP(z,t)$ over depth (panel 2D) and over time (panel 2F). $E(z,t)$ and $PP(z,t)$ peak at noon and diminishes with depth, while $QY(z,t)$ displays an opposite pattern since it decreases with irradiance. Note that Figure 2 only displays the upper 5 m of water column for clarity, as there is only minimal change below 3 m depth, while the actual calculations extended to 10 m depth. The differences in other seasons are even less pronounced, demonstrating strong light absorbance in the surface layers, even at medium to high salinity.

2.4 Nutrient concentration

TOC and total nitrogen (TN) were analysed by high-temperature catalytic oxidation and non-dispersive infrared detection on a Shimadzu TOC-VCPH Analyzer connected to a TNM-1 Total Nitrogen Measuring Unit (Shimadzu scientific instruments, Columbia, Maryland, United States). The CO_2 and NO gasses evolving from the water samples after heating to 680°C with platinum catalyst were cooled and dehumidified before detection. Concentrations of TOC/TN were obtained through comparison with a calibration curve.

Particulate N was also measured by firstly filtering sample water through 0.7 µm pore size GF/F glass fiber filters, and then combusting the filters in a FlashEA 1112 Nitrogen and Carbon Analyzer (Thermo Fisher Scientific). The resulting gas in the apparatus was analysed on elemental composition by gas chromatography. Dissolved N was calculated as a difference between TN and particulate N.

2.5 Statistical analysis

Linear models were used to test the relationships between the variables, while ANOVAs were used to test for significance in variables change across salinity and seasons. Statistical tests were conducted using R (version 4.3.1; R Core Developer Team 2024). All the calculations are based on a dataset of 34 samples (n = 34). Figure 1 was created using Stamen maps (Kahle and Wickham, 2013).

The analytical uncertainty is minimal for CDOM absorption measurements ($\overline{a_{CDOM}}$), with SD between PAR-averaged (400–700 nm) absorption coefficients of MilliQ water blanks being ±0.025 m^{-1} (n = 3). Control runs of filter blanks using integrating sphere method ($\overline{a_p}$ and $\overline{a_d}$ at 400–700 nm) resulted in similar uncertainty level (SD = ±0.026 m^{-1}, n = 4).

10.3389/fphbi.2024.1452747

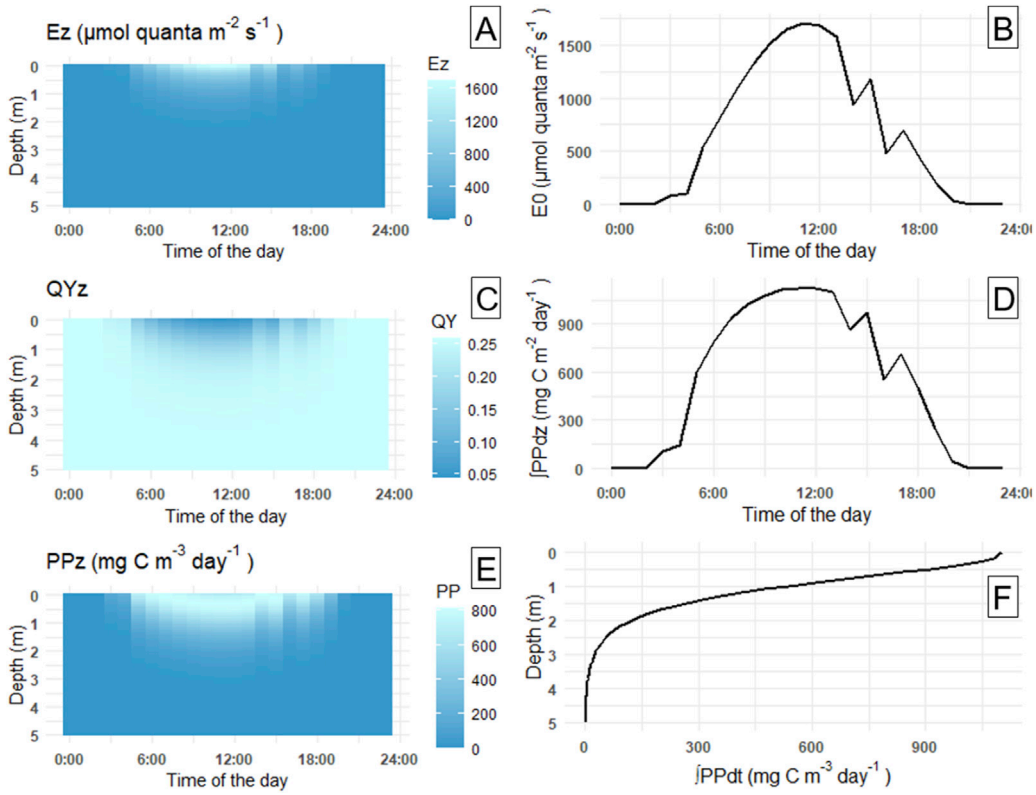

FIGURE 2
(A) Irradiation at depth z (E_z) in the upper 5 m layer (µmol quanta m^{-2} s^{-1}); **(B)** Surface irradiance (E0) throughout the sampling day (µmol quanta m^{-2} s^{-1}); **(C)** Quantum yield at depth z (QY_z); **(D)** Bio-optically estimated PP integrated over depth z [$\int$PPdz (mg C m^{-2} day^{-1})]; **(E)** PP at depth z [PP_z (mg C m^{-3} day^{-1})]; **(F)** PP integrated over time [$\int$PPdt (mg C m^{-3} day^{-1})].

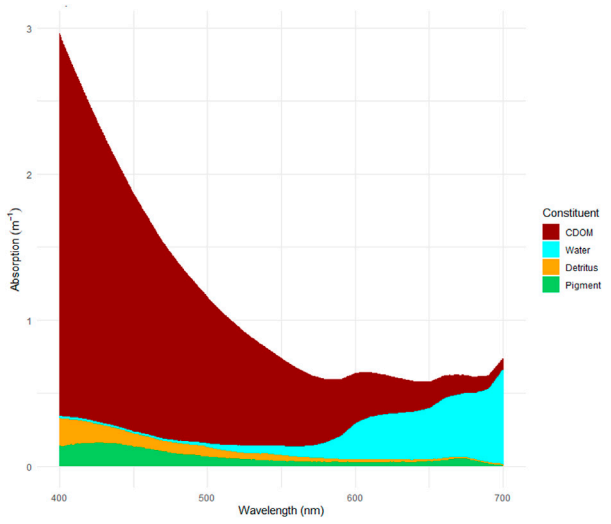

FIGURE 3
Cumulative absorption coefficients (m^{-1}) by four absorbing constituents [a_{CDOM} (λ), a_p (λ), a_d (λ) and a_{H2O} (λ)] at PAR spectrum. This is an example of absorption in a single sample (station I1, 17.06.2021), see Supplementary Figure 3 for the rest of the samples.

3 Results

3.1 Absorption by the four constituents

The relative contribution of absorption of the four components shows substantial spectral differences, with CDOM and particles increasing strongly towards shorter wavelengths (Figure 3; Supplementary Figure 3). CDOM contributed by far most of the wavelength-integrated PAR absorption relative to particles, phytoplankton and water through stations and season, including the outermost, most marine station (Figure 4). PAR attenuation contribution from CDOM ($\overline{F_{CDOM}}$) insignificantly decreased with salinity (Supplementary Table 1) yet constituting 50%–80% of total absorption at all stations (~67%; Supplementary Figure 4B). The one outlier L5, 25.03.2021, had $\overline{F_{CDOM}}$ of just 40%, however even in this case CDOM remained the major contributor to total absorption. A strong inverse relationship between PAR-averaged CDOM absorption and salinity was present, while seasonality did not play a significant role in distribution of CDOM across the measured gradient (Figure 5; Supplementary Table 1).

Phytoplankton contributed around 1%–25% of absorption in upper water layers, depending on the season and location in the fjord

10.3389/fphbi.2024.1452747

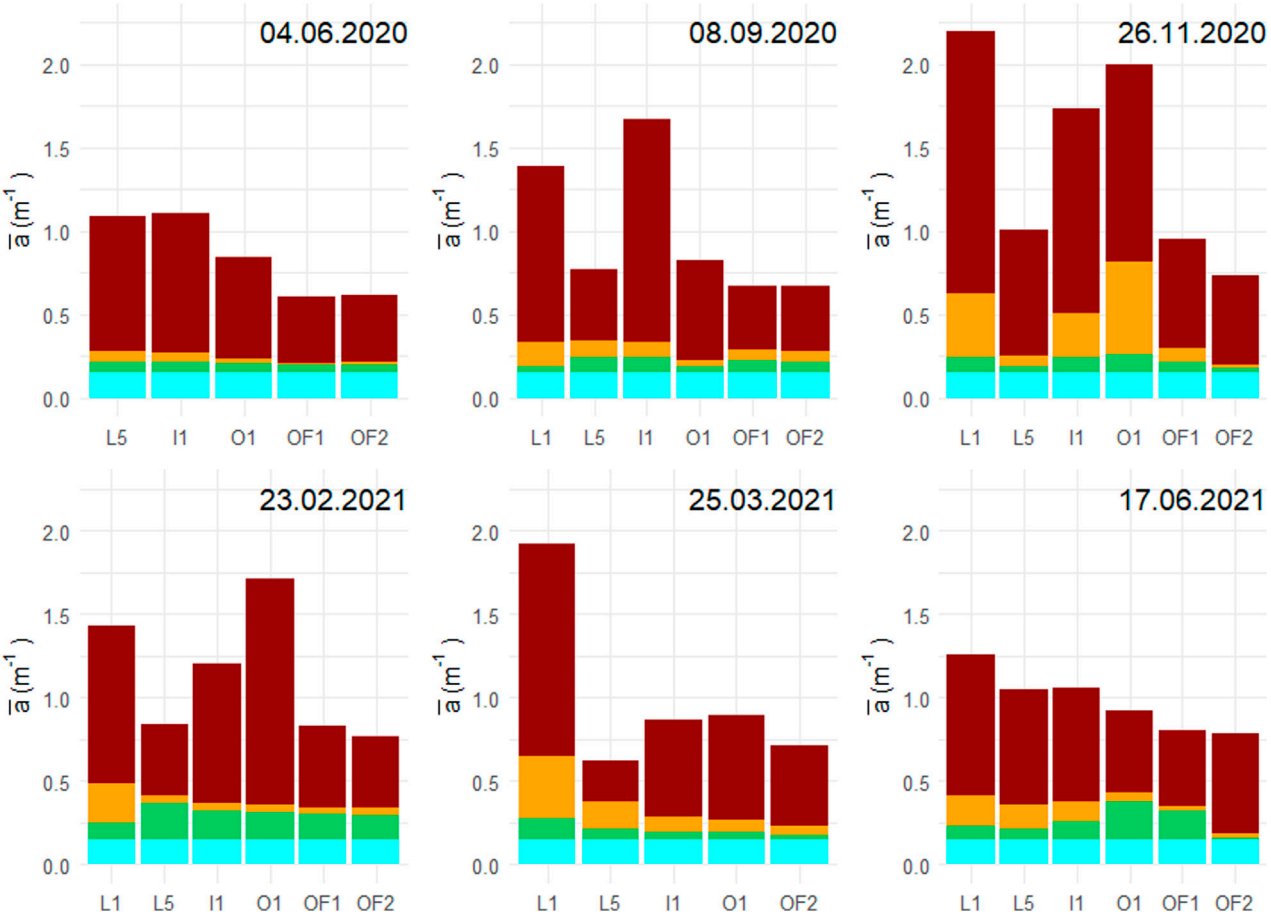

FIGURE 4
PAR spectrum integrated absorption (m^{-1}) at the six sampling stations grouped by sampling dates. The four absorption constituents were CDOM (dark red), detritus (orange), pigments (green) and water (blue).

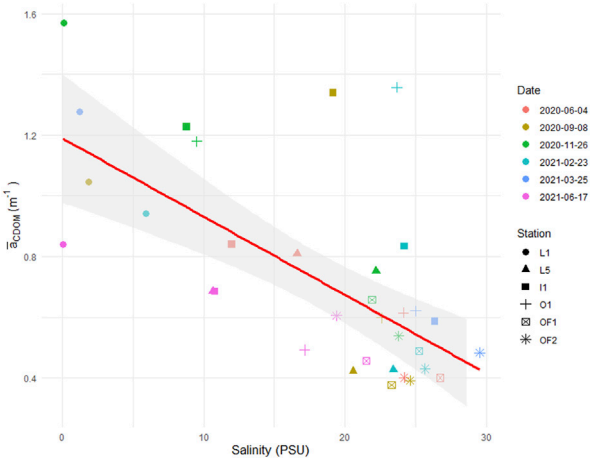

FIGURE 5
The relationship between salinity (PSU) and PAR-averaged absorption coefficient of CDOM (m^{-1}).

(Figure 4). PAR-averaged *in vivo* pigment absorption measurements show two distinct trends when plotted against salinity (Supplementary Figure 4C). June 2020, November and March samplings show a decrease in $\overline{a_p}$ with increasing salinities, whereas September, February and June 2021 saw an increase of $\overline{a_p}$ over the salinity range. There are therefore statistically significant deviations in $\overline{a_p}$ between the seasons. $\overline{a_p}$ values at the marine sites were very similar for most seasons, with the exception of February—the most productive season, which were substantially higher, and mid-June 2021, when there was huge site to site fluctuations. $\overline{a_p}$ were more variable at the freshwater end of the gradient, but without clear division of high and low $\overline{a_p}$ seasons, whereas marine samples clearly divide into those two categories.

Detritus, being the particulate fraction of TOC, follows the mixing trend of CDOM, as the PAR-averaged absorption coefficient of detritus ($\overline{a_d}$) decreases along salinity gradient (Supplementary Figure 4E). $\overline{F_d}$ was ~8%, yet ranging from 1% to 27% of total absorption. $\overline{a_d}$ was also significantly influenced by the seasonality in the area, with March having the highest combined $\overline{a_d}$ and June 2020 having the minimal $\overline{a_d}$. The contribution from detritus to total absorption matches that of phytoplankton (~9%), however while detritus have a higher fraction of absorption at inner, more freshwater-impacted stations, the $\overline{F_p}$ increases with salinity. PAR-averaged water absorption ($\overline{a_{H2O}}$) was considered to be constant irrespective of salinity, however if we consider fraction of total absorption by water ($\overline{F_{H2O}}$), there is a strong positive linear

10.3389/fphbi.2024.1452747

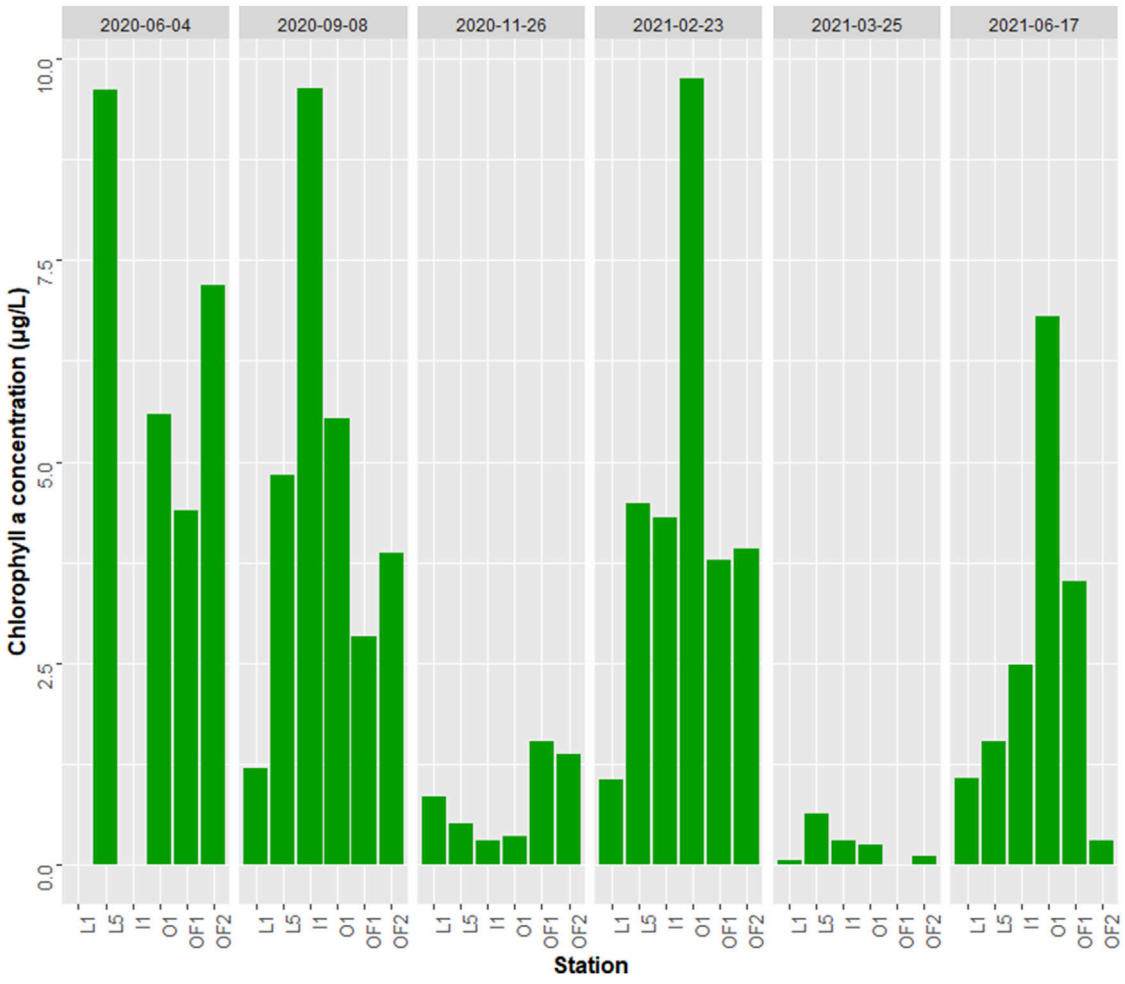

FIGURE 6
Chlorophyll *a* concentrations (µg/L) at stations and grouped by sampling dates. The stations order represents the gradient of increasing salinity from L1 to OF2.

correlation with salinity (Supplementary Figure 4H), primarily reflecting a decreased absorption by the other three constituents.

CDOM absorbs primarily at shorter wavelengths, with a log-linear decrease of $a_{CDOM}(\lambda)$ with wavelength (Figure 3). Violet-blue light is absorbed by all photosynthetic pigments, however there are additional peaks of $a_p(\lambda)$in other parts of PAR depending on the pigments (Yacobi, 2012). Pigment absorption peaked at around 670 nm and 430 nm, which is characteristic for chl*a* (Supplementary Figure 5). Two smaller peaks were also present at the yellow-orange part of the spectrum (580 and 630 nm), which corresponds to absorption signature of carotenoids and chlc_2. The relative contribution of water to total absorption gets progressively higher from shorter to longer wavelengths (Figure 3).

3.2 Chlorophyll *a* concentrations

Chlorophyll *a* (chl*a*) peaked during June 2020, when it averaged 6.7 µg/L (Figure 6), followed by September and February with concentrations of 4.6 and 4.5 µg/L respectively. The second summer season, June 2021, had however less than half of chl*a* concentration of its 2020 counterpart (2.6 µg/L). The lowest chl*a* concentration seasons were November and March (0.8 and 0.3 µg/L respectively).

There was no definitive trend of chl*a* concentration distribution across the salinity transect, although L1, the inner station, generally had the lowest chl*a* concentrations compared to more open water stations on most sampling dates. Both open sea (OF1 and OF2) and intermediate stations (L5, I1 and O1) have comparable chl*a* concentrations, with seasonality determining the spatial patterns of peak phytoplankton concentration. Chl*a* concentration and $\overline{a_p}$ were positively correlated (Supplementary Table 2), yet with a pronounced scatter (Supplementary Figure 6A).

3.3 Bio-optical primary production estimates

Most of the PP estimates lie below 1,000 mg C m^{-2} day^{-1} (Figure 7). There are three very high values exceeding 1,000 mg C m^{-2} day^{-1}, all recorded on the 17.06.2021 sampling. The broad fluctuation in PP values between the sites on this date was mainly

10.3389/fphbi.2024.1452747

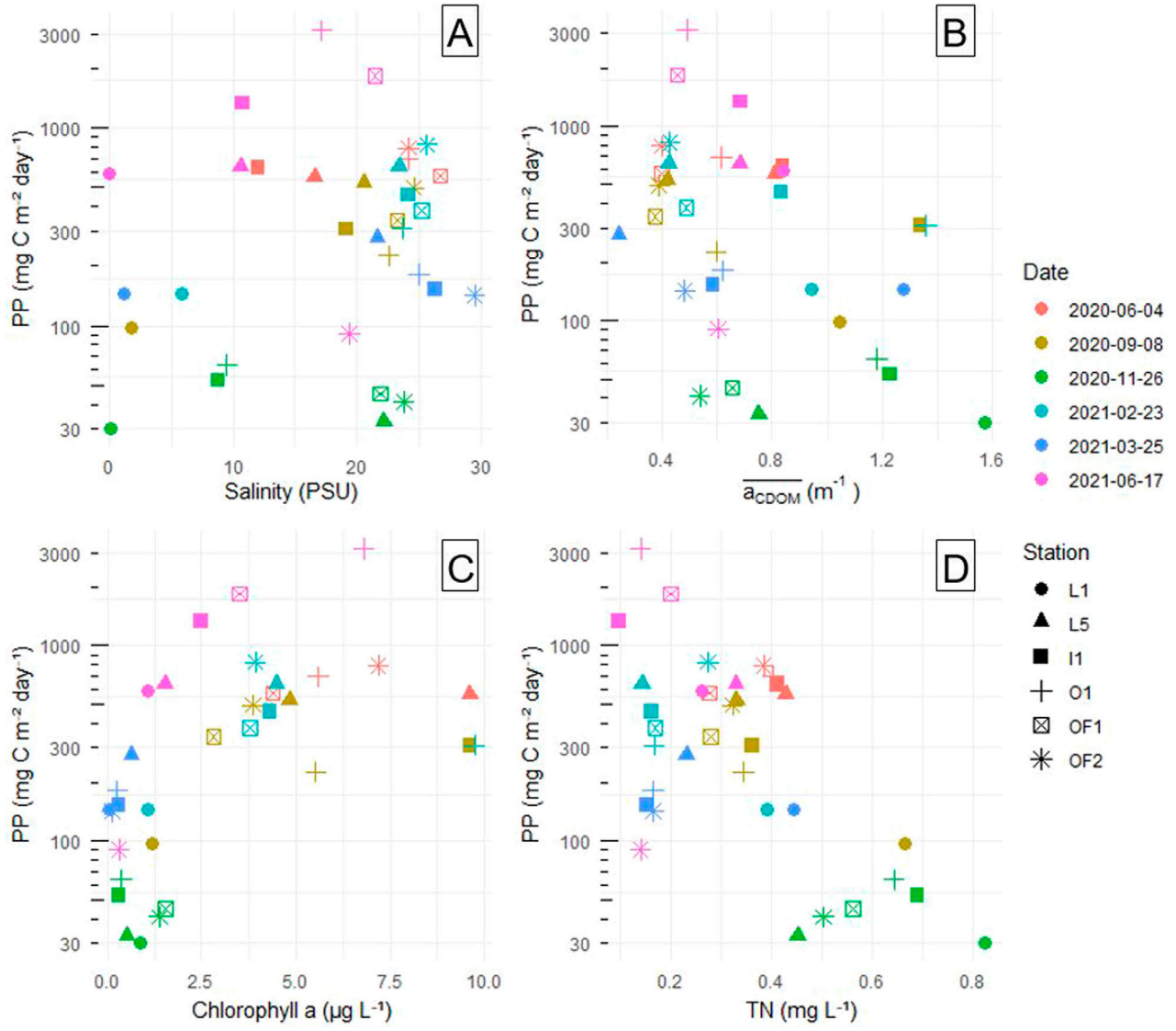

FIGURE 7
Relationship between log (10) transformed PP (mg C m^{-2} day^{-1}) and **(A)** salinity (PSU), **(B)** PAR-averaged CDOM absorption (m^{-1}), **(C)** chl*a* concentration (µg/L) and **(D)** TN concentration (mg/L). Datapoints are grouped by shapes (stations) and colours (sampling dates).

due to non-uniform distribution of phytoplankton across the sampling transect. 17.06.2021 saw the highest mean PP of all dates (1,270 mg C m^{-2} day^{-1}), almost twice that of the second highest PP recording on 04.06.2020. It was also sunny prior to the sampling date in June 2020, but pigment absorption was considerably lower. The February maximum in chl*a* concentrations and pigment absorption coefficients did not translate to maximal PP (only 180 mg m^{-2} day^{-1} on average), likely due to the low winter irradiation (Supplementary Figure 7). March and September samplings had comparatively higher PPs (460 and 333 mg m^{-2} day^{-1} respectively), despite lower chl*a* concentrations. Primary production reached its minimum in November, when phytoplankton numbers were dwindling and solar irradiation was low (44 mg m^{-2} day^{-1} on average). Overall, E_0 and $\overline{a_p}$ seem to be the best predictors to PP, with a higher degree of correlation than with $\overline{a_{CDOM}}$ and salinity (Figure 7, Supplementary Table 1). Counterintuitively, TN is in inverse proportion to PP, however, this might be primarily an effect of CDOM (see *Discussion*).

Yet another important variable influencing PP was QY_0 (quantum yield at $E = 0$). We fitted a log-linear model of QY as function of E, with a common slope and additive effects of sampling date and station on the intercept. The model explained only 29% of the total variance but gave a reasonably precise estimate of the common slope (Supplementary Figure 7). If we write the model as $QY\ (E) = QY0 \exp(-E/E')$ then the estimate for E' becomes 933 µmol quanta m^{-2} s^{-1} (95% CI = [648, 1,670]). Figure 8 shows the seasonal variation in the estimated intercept (QY at $E = 0$). QY_0 estimates generally were under 0.5 mark, with the exception of February, when QY_0 reached 0.6 (Figure 8). QY_0 correlated well with chl*a* concentration, approximately following the same seasonal trend.

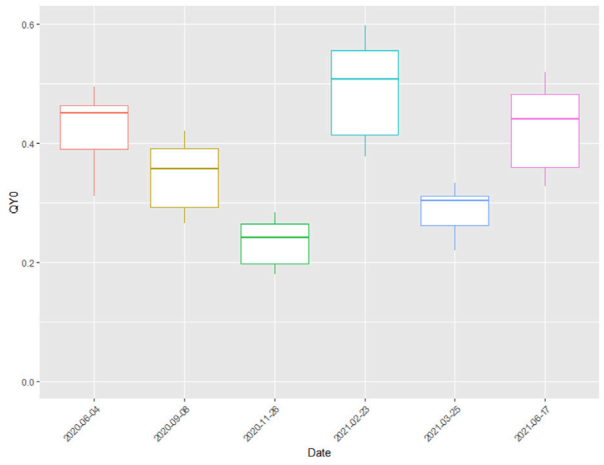

FIGURE 8
Quantum yields of photosystem II at E = 0 (QY_0), grouped by sampling dates.

3.4 Nutrient concentrations

The very early spring bloom (which typically occurs in late February to mid-March in the fjord) can be attributed to high nutrient concentrations, in addition to water column stability due to low average wind speeds as well as low freshwater inflow (NCCS, 2024; Supplementary Figure 1). Nitrogen followed conservative mixing (Supplementary Figure 9A), and the highest concentrations of TN were recorded in November (Figure 7D), when nitrogen have accumulated after the autumn bloom, however there is insufficient light to support phytoplankton production. An increase in chl*a* concentration was observed at the marine stations in late February in conjunction with a fast depletion of TN concentrations (to 0.14–0.27 mg/L levels, as opposed to 0.45–0.69 mg/L in November; Figure 7D). The same trend was not seen in the inner, riverine station however, where TN concentrations were consistently higher than in the outer stations due to constant supply of riverine water. The fluctuations in TN related to PP should be judged with caution however, since TN also includes the particulate and organic fractions of N. TN was consisting on average of 87% of dissolved N (ranging from 60% in June 2021 to 97% in November). TN levels stayed at similar levels throughout March (0.15–0.23 mg/L) and decreased over the spring to June 2021 levels, when the average TN concentration among all stations was the lowest (0.19 mg/L). There is a stark contrast between June 2020 and June 2021 TN averages (0.38 and 0.19 mg/L accordingly).

TOC concentrations (Supplementary Figure 6B) were quite similar at marine stations in February, March, June 2020 and September (1.91–2.95 mg/L). The riverine station consistently had the highest TOC concentrations measured on any single day, marking Glomma as a source of OM in the studied area. June 2021 had the highest mean TOC concentration (3.80 mg/L) and PP on that day was exceedingly high. Moreover there was a small degree of fluctuation in TOC concentrations between all 6 stations (3.60–4.00 mg/L), hinting at the estuary being horizontally well-mixed this time of year. November had the second highest TOC levels that were accumulated during autumn, which in conjunction with absence of chl*a* contributed to low PP.

4 Discussion

4.1 Attenuation coefficients

As a result of non-phytoplankton attenuation, the euphotic zone (1% of surface PAR penetration) in the Norwegian coastal waters is reduced to around 14 m, while being 112 m deep in the clear North Atlantic Ocean (Aksnes, 2015). CDOM enrichment of an aquatic system will lower the compensation depth, and narrow the euphotic zone thereby reducing the area-specific primary production. CDOM was found to consistently be the dominant contributor to attenuation of downwelling PAR in the Oslofjord, influencing the estimated PP. Sverdrup's critical depth is the depth interval over which integral phytoplankton growth matches losses (Sverdrup, 1953). This critical depth influences also the onset of the spring phytoplankton bloom, such that changes in critical depth can lead to changes in bloom timing (Opdal et al., 2019; Diehl et al., 2015). Terrestrially derived compounds may make euphotic zone shallower, thus playing a major role for light climate and photosynthesis in coastal areas.

Both $\overline{a_{CDOM}}$ and $\overline{a_d}$ show linear decrease with salinity (Figure 5, Supplementary Figure 4E). Unlike $\overline{a_p}$, the organic matter mixing pattern is consistent between seasons. Nevertheless, there is low correlation between $\overline{a_{CDOM}}$ and $\overline{a_d}$, i.e., seasons with high $\overline{a_{CDOM}}$ do not correspond to high a_d. $\overline{F_{CDOM}}$ stays mostly constant throughout the salinity range, even though $\overline{a_{CDOM}}$ decreases. As all constituents, excluding water, CDOM absorbs less light in open sea, yet it remains the major absorber even at the most offshore station. Absorbance by the particulate detritus fraction, $\overline{F_d}$, decreased with salinity, likely reflecting sedimentation or breakdown of particulate matter towards open waters. Decreasing $\overline{F_d}$ would result in increasing $\overline{F_{CDOM}}$, if not for the compensation effect of increasing $\overline{F_{H2O}}$ at higher salinities. $\overline{a_d}$ was also significantly related to seasonality, unlike CDOM, suggesting that the amount detritus carried from the river mouth is more dependent on discharge driven by snowmelt or rainfalls. Still, $\overline{a_{CDOM}}$ is continuously decreasing offshore due to progressive dilution plus microbial and/or solar breakdown (Chen et al., 2015; Dempsey et al., 2020). Photobleaching has been shown to increase the rate of TOC loss with decreasing pH. Simultaneously, when pH is over 7 and increasing, photodegradation reduces colour of CDOM more rapidly (Williamson et al., 2014). Since salinity directly affects pH, photodegradation is an important factor influencing DOC throughout the estuarine salinity gradient.

$\overline{a_p}$ has two contrasting trends when tested against salinity, it could be explained by the patterns of distribution of phytoplankton in the outer Oslofjord (Supplementary Figure 4C). There is a cluster of $\overline{a_p}$ data points between 20 and 30 PSU, shared between the four sampling dates. It seems that phytoplankton is always present at low abundances (between 0.025 and 0.075 m^{-1}) in open sea, with a substantial peak during late winter to early spring bloom (i.e., February with ~ 0.175 m^{-1}). This shows how seasonality plays an important role in the study area, which is typical for a temperate sea (Acevedo-Trejos et al., 2015). Stratification and temperature changes are known to impact the magnitude and

succession of phytoplankton blooms greatly (Berger et al., 2010). The most productive season (February) shows increase of $\overline{a_p}$ with salinity, but this is mainly due to the outer sea having a deep pycnocline this time of year, with all outer and intermediate stations having similar salinities and abundant nutrients, making the freshwater station a less favorable site for photosynthesis in comparison.

4.2 Chlorophyll *a* concentrations

Our study found high chl*a* concentrations in late February and low concentrations in late March, indicative of a very early spring bloom. This is consistent with the onset of spring phytoplankton bloom in the Oslofjord (Braarud, 1969; Lundsør et al., 2020). Moreover, *Skeletonema* spp. have even been observed to bloom as early as January in the Oslofjord (Dittami et al., 2013). The spring bloom in the fjord is always early, yet variable, and may also occur in late March (Poste et al., 2021). The fjord typically has a second spring bloom in May-June, which can be seen in the amplified June chl*a* levels (Figure 7C). The captured early spring bloom seems like an outlier in the progressively delayed onset of spring bloom trend that was observed in Norwegian coastal waters over the last century (Opdal et al., 2019; Lundsør et al., 2022). Lundsør et al. (2020) reported decreasing chl*a* concentrations since 1970s, when chl*a* levels during spring bloom were reaching 20 µg/L to under 6 µg/L concentrations in the 2010s. Our study revealed an average of 4.5 µg/L during the bloom season (Figure 6), reflecting the reduction of nutrient efflux to the fjord and possibly also increasing grazing pressure from smaller zooplankton (180–1,000 µm) in early spring associated with higher temperatures (Lundsør et al., 2021).

Chl*a* was lowest in the innermost, river impacted station, while intermediate sites generally had the highest chl*a* concentration. This could reflect two contrasting drivers: CDOM-load and nutrient availability. While nutrients are more abundant in near-shore environments and get diluted further out in the sea, the darkening associated with CDOM is also the highest in the innermost station and could override the impact of nutrient supply (Lyche Solheim et al., 2024). The darkening effect of river water on chl*a* concentrations seems to be stronger than the accompanying nutrient availability, meaning that there is a net negative impact on the marine primary production of the CDOM-rich freshwater input. This is in support of studies from freshwater, suggesting a break-point with a transition from positive to negative impact on primary production with increased CDOM (Karlsson et al., 2009; Thrane et al., 2014).

4.3 Bio-optical primary production estimation

The estimates of PP based on the bio-optical model in general yielded rates comparable to previous estimates based on radiolabelling (^{14}C; Smith et al., 1989). The reason for the very high PP of the three extreme values (I1, OF1 and O1 on 17.06.2021) was relatively clear water (high $\overline{F_p}$ and low $\overline{F_{CDOM}}$) and intense sunshine. At the same time phytoplankton abundance (both pigment concentration and absorbance) was not particularly high, hinting at the importance of CDOM in limitation of photosynthesis. The fluctuations in PP between the stations on that day were large due to varied pigment absorption coefficients. High $\overline{a_p}$ measured on some station (I1, OF1 and especially O1) combined with high surface irradiance values resulted in particularly high PP. Coincidentally, chl*a* concentrations were not out of ordinary for these data points (Figures 7B, C). This suggests that the reason for the very high PP could be low absorption by other absorbing elements (Figure 4), leaving more light available for photosynthesis. High production at comparatively low phytoplankton biomass in June could indicate high turnover rate.

The difference that bright sun makes is reflected in PP values from February. Pigment concentrations and absorption in February were both particularly high, but the resulting PP values were in line with those seen in other seasons. Effective photosynthesis at other seasons, however, was limited more by pigment and quantum yield of PSII, rather than by light *per se* (i.e., September and March). When comparing to previous literature on productivity in the Oslofjord, peak PP of 3 g C m^{-2} day^{-1} in the current study resembles peak PP measured in the inner fjord in 1974 (2.8 g C m^{-2} day^{-1}; Throndsen, 1978). Both peaks occurred in June. Average May PP in the Kattegat-Skagerrak area (where the outer fjord falls into) varied from 575 to 908 mg C m^{-2} day^{-1} in 1987–1993 (Heilmann et al., 1994), while our average PP estimates in June 2020 and 2021 are 650 and 1,271 mg C m^{-2} day^{-1} respectively. We did not find a linear increase in PP with salinity, possibly due to both salinity and seasonality contributing to the fluctuations in PP. For example, low productivity November and high productivity June had good spread of salinities, but similar PP levels among the stations, flattening out the common trend (Figure 7A).

A study of a long, 110 km salinity gradient in a Greenland fjord found that PP increases 10-fold from turbid inner to marine outer fjord (Sejr et al., 2022). Same goes for $\overline{a_{CDOM}}$ – PP correlation, there are high and low discharge seasons translating into seasonal separation of $\overline{a_{CDOM}}$ (Figure 5; Supplementary Figure 1). Nevertheless, a weak trend of reduction of PP with increase $\overline{a_{CDOM}}$ can be observed (Figure 7B). Contrary to this, a controlled mesocosm experiment showed that PP is not influenced by brownification to a significant degree (Spilling et al., 2022). However, they highlighted that phytoplankton community composition shifted towards smaller species. In their study, nutrient enrichment stimulated plankton growth in both clear and murky water; however, another study by Lyche Solheim et al. (2024) reports that browning counteracts positive effects of nutrients. In this case, the plankton community underwent changes, with mixotrophic cryptophytes outcompeting cyanobacteria and chlorophytes. The ecological impacts of CDOM enrichment on phytoplankton may therefore be less obvious than a straightforward competition for photons with dissolved matter. Moreover, our model included only PAR irradiance, excluding harmful UV irradiation from the equation. CDOM absorbs the most light in UV spectrum, thereby shielding plankton from some of the harmful UV radiation. In fact, CDOM presence was even reported to enhance primary productivity in the shallow water (<30 m) due to this effect, counteracting the reduction of photosynthetically useable radiation (Arrigo and Brown, 1996).

Calculated PP in June 2021 were generally higher than that of June 2020. This could be attributed to the fact that June

2021 sampling was done after heavy freshwater influx from the main inlet, the Glomma River, while June 2020 sampling was set right at the beginning of the flood. Nutrients were therefore more available for the phytoplankton in the later year, which reflected on much greater E_{pp} values especially at the outer sites. Another reason for much higher E_{pp} in 2021 is light conditions—substantially sunnier weather in the later year (average E_0 of 530, as opposed to 411 µmol/m^2/s). The only exception to the rule was OF2 station, one of the more open sea stations, where pigment absorption during the winter was minimally higher than the June 2020 counterpart. QY_0 was quite similar between the two seasons and have likely not contributed to the variability of PP much (Figure 8).

Bio-optical PP estimation method relies on absorbance measurements and is thus affected by the associated uncertainties such as photon scattering in the spectrophotometer (Kirk, 1994) and discrepancies in fluorometry measurements (e.g., imperfect dark exposure prior to PAM measurements, leading to relatively low *QY0* values). Additionally, PP tends to be overestimated due to the assumption that CO_2-fixation is proportional to the electron transport rates, which, in practice differ depending on phytoplankton species and environmental factors (Lawrenz et al., 2013). Another source of overestimated PP values could be the fact that we use a theoretical factor of 0.08 (1/12) of mol CO_2 fixed per mol of photons absorbed (Kirk, 1994), while in reality this factor is closer to 0.03–0.05 mol C per mol photons in eutrophic waters (Babin et al., 1996). However, conventional isotope uptake methods also come with some assumptions and challenges, particularly due to the enclose effect (*cf.* Gieskes et al., 1979; Peterson, 1980). Fluorescence measurements for bio-optical PP estimation are convenient, rapid and continuous, without the need for incubations, thus avoiding the "bottle effects" (Kolber and Falkowski, 1993). The bio-optical PP model is also advantageous because parameters, such as absorbance in the water column, PAR penetration and phytoplankton production are mechanistically linked (Smith et al., 1989).

4.4 Nutrients

PP in temperate coastal waters is most commonly N-limited (Howarth and Marino, 2006), or eventually co-limited with phosphorus (Andersen et al., 1991; Elser et al., 2007). The nutrient analysis in our study should be judged with some caution, since N-species and the fractions or concentrations of DIN was not analyzed. However, N-limitation seems to be prominent in the Oslofjord (Lundsør et al., 2020), and this is known to lower the photochemical energy conversion efficiency of PSII (Kolber et al., 1988). This might thus have had a negative effect on QY's seen in the current study (Figure 8). Late autumn and early spring were the two least optimal seasons for photosynthetic activity. While low phytoplankton production in November was mainly attributed to low solar irradiation, PP in March was possibly stifled by low nitrogen availability (Figure 7D). And while February and March N concentrations are on par, the late February sampling captured the peak of phytoplankton bloom when the nutrients were already depleted, but the phytoplankton concentrations were still high. The relation between total N and phytoplankton should however be judged with caution. PP being negatively correlated to N concentration could in fact be an effect of CDOM in disguise (Supplementary Figure 9B), due to dissolved organic N associated with CDOM (e.g., Lyche Solheim et al., 2024). As TN is dominated by dissolved N ($\bar{x}$ = 87%), the TN dynamics is not due to particulate N. The stark differences between June 2020 and June 2021 TN concentrations can be attributed to different timing of phytoplankton blooming.

Nitrogen in the outer Oslofjord in 2020 was mainly of natural origin (38%), followed by runoff from agriculture (34%), population (24%) and industry (3%; Walday et al., 2023). A significant increase in TN transport in Glomma has been observed since 1999, with average annual increase of 108 tonnes per year (Kaste et al., 2022). While nitrate transport still increases at a rate of plus 47 tonnes per year, ammonia transport saw a reduction (−17.2 tonnes per year), likely due to reduced air pollution and increased vegetation uptake (as a result of global warming driven greening). Nitrogen is bioavailable primarily as dissolved, inorganic nitrogen, nitrate or ammonia. Riverine nutrient loading promotes light attenuation not only by directly increasing particles that absorb light, but also indirectly by stimulating algal growth (Wallhead et al., 2021). A total of 15,007 tonnes of nitrogen were transported in 2020 from Glomma into the studied area of which 10,136 tons was NO_3 and 192 tons was NH_4 (68% and 1% respectively; Kaste et al., 2022). This means that the Glomma freshwater had an average daily concentrations of 511 µg/L of TN influencing the coastal ecosystems, of which the major part was inorganic (336 µg/L of NO_3 and 7.6 µg/L of NH_4). Riverine water held high concentrations of organic carbon–4.2 mg/L of TOC (120149 tonnes in 2020), most of which was likely terrestrially-derived DOM, contributing to coastal darkening directly. Additionally, a loading of 384 tonnes of PO_4 was recorded, which likely also promoted phytoplankton growth.

4.5 Conclusion

Among all the four major light absorption components in the water column (CDOM, pigment, detritus and water), CDOM consistently was the major light absorber in the PAR spectrum, increasing towards shorter wavelengths. DOM contributed 50%–80% of total absorption of integrated PAR in coastal waters of the Oslofjord across season and station along a salinity gradient (0–30 PSU). PAR-averaged CDOM absorption showed a significant inverse relationship with salinity; however, relative absorption fraction by CDOM remained mostly constant. CDOM played an important, but not the main role in regulating PP estimates derived from the bio-optical model. PP estimates were primarily controlled by pigment absorption and concentration, quantum yield of PSII and light intensity. The bio-optical model produced realistic PP estimates, consistent with previous measurements conducted in the area. PP in the area exhibited substantial seasonal variability ranging from 30 to about 3,000 mg C m^{-2} day^{-1}, as well as a weak salinity signal. The highest pigment absorption and chlorophyll *a* concentrations observed in late February indicate an early spring bloom.

Data availability statement

The original contributions presented in the study be found in the Figshare repository https://doi.org/10.6084/m9.figshare.28070933.

Author contributions

AB: Conceptualization, Data curation, Formal Analysis, Investigation, Methodology, Visualization, Writing–original draft. DH: Conceptualization, Funding acquisition, Project administration, Resources, Supervision, Validation, Writing–review and editing. TA: Conceptualization, Methodology, Supervision, Validation, Visualization, Writing–review and editing.

Funding

The author(s) declare that financial support was received for the research, authorship, and/or publication of this article. This work was supported by Norges Forskningsråd. Grant Number: TerraCoast 287490.

Conflict of interest

The authors declare that the research was conducted in the absence of any commercial or financial relationships that could be construed as a potential conflict of interest.

Publisher's note

Supplementary material

The Supplementary Material for this article can be found online at: https://www.frontiersin.org/articles/10.3389/fphbi.2024.1452747/full#supplementary-material

SUPPLEMENTARY FIGURE 1
Daily average Glomma discharge volumes including the 6 sampling dates (NVE Sildre, 2024).

SUPPLEMENTARY FIGURE 2
Comparison between the fully spectrally resolved and PAR-averaged coefficient-based bio-optical models.

SUPPLEMENTARY FIGURE 3
Cumulative absorption coefficients (m^{-1}) by four absorbing components [a_{CDOM} (λ), a_p (λ), a_d (λ) and a_{H2O} (λ)] at PAR spectrum of all the analysed samples. Cruises 1–6 correspond to sampling dates.

SUPPLEMENTARY FIGURE 4
The relationships between salinity (PSU) and **(A)** absorption coefficient of CDOM (m^{-1}); **(B)** fraction of absorption by CDOM; **(C)** absorption coefficient of pigment (m^{-1}); **(D)** fraction of absorption by pigment; **(E)** absorption coefficient of detritus (m^{-1}); **(F)** fraction of absorption by detritus; **(G)** total attenuation coefficient, which is the sum of the three previously mentioned elements and water (m^{-1}); **(H)** fraction of absorption by water. All of the absorption coefficients and fractions of absorption are PAR-averaged (400–700 nm).

SUPPLEMENTARY FIGURE 5
In vitro pigment absorption (m^{-1}) spectra of all samples plotted against wavelength (nm).

SUPPLEMENTARY FIGURE 6
Relationships between **(A)** PAR-averaged pigment absorption (m^{-1}) and chl*a* concentration (µg L^{-1}), **(B)** PP (mg C m^{-2} day^{-1}) and TOC concentration (mg L^{--1}).

SUPPLEMENTARY FIGURE 7
Sum of PAR irradiation (mol quanta m^{-2} day^{-1}). This is an example for the coordinates of O1 station. Data from STRÅNG (2024).

SUPPLEMENTARY FIGURE 8
Relationship between light intensity (*E*, µmol quanta m^{-2} s^{-1}) and QY.

SUPPLEMENTARY FIGURE 9
Relationships between TN (mg/L) and **(A)** salinity (PSU), and **(B)** PAR-averaged CDOM absorption (m^{-1}).

References

Acevedo-Trejos, E., Brandt, G., Bruggeman, J., and Merico, A. (2015). Mechanisms shaping size structure and functional diversity of phytoplankton communities in the ocean. *Sci. Rep.* 5 (1), 8918. Article 1. doi:10.1038/srep08918

Aksnes, D. L., Nejstgaard, J., Sædberg, E., and Sørnes, T. (2004). Optical control of fish and zooplankton populations. *Limnol. Oceanogr.* 49 (1), 233–238. doi:10.4319/lo.2004.49.1.0233

Aksnes, D., Dupont, N., Staby, A., Fiksen, Ø., Kaartvedt, S., and Aure, J. (2009). Coastal water darkening and implications for mesopelagic regime shifts in Norwegian fjords. *Mar. Ecol. Prog. Ser.* 387, 39–49. doi:10.3354/meps08120

Aksnes, D. L. (2015). Sverdrup critical depth and the role of water clarity in Norwegian Coastal Water. *ICES J. Mar. Sci.* 72 (6), 2041–2050. doi:10.1093/icesjms/fsv029

Allesson, L., Valiente, N., Dörsch, P., Andersen, T., Eiler, A., and Hessen, D. O. (2022). Drivers and variability of CO2:O2 saturation along a gradient from boreal to Arctic lakes. *Sci. Rep.* 12 (1), 18989. doi:10.1038/s41598-022-23705-9

Andersen, T., Schartau, A. K. L., and Paasche, E. (1991). Quantifiying external and internal nitrogen and phosphorus pools, as well as nitrogen and phosphorus supplied through remineralization, in coastal marine plankton by means of a dilution technique. *Mar. Ecol. Prog. Ser.* 69, 67–80. doi:10.3354/meps069067

Arrigo, K. R., and Brown, C. W. (1996). Impact of chromophoric dissolved organic matter on UV inhibition of primary productivity in the sea. *Mar. Ecol. Prog. Ser.* 140 (1/3), 207–216. doi:10.3354/meps140207

Babin, M., Morel, A., Claustre, H., Bricaud, A., Kolber, Z., and Falkowski, P. G. (1996). Nitrogen- and irradiance-dependent variations of the maximum quantum yield of carbon fixation in eutrophic, mesotrophic and oligotrophic marine systems. *Deep-Sea Res. I: Oceanogr. Res. Pap.* 43 (8), 1241–1272. doi:10.1016/0967-0637(96)00058-1

Berger, S. A., Diehl, S., Stibor, H., Trommer, G., and Ruhenstroth, M. (2010). Water temperature and stratification depth independently shift cardinal events during plankton spring succession. *Glob. Change Biol.* 16 (7), 1954–1965. doi:10.1111/j.1365-2486.2009.02134.x

Blain, C. O., Hansen, S. C., and Shears, N. T. (2021). Coastal darkening substantially limits the contribution of kelp to coastal carbon cycles. *Glob. Change Biol.* 27 (21), 5547–5563. doi:10.1111/gcb.15837

Braarud, T. (1969). *Pollution effect upon the phytoplankton of the Oslofjord*. ICES.

Bricaud, A., and Stramski, D. (1990). Spectral absorption coefficients of living phytoplankton and nonalgal biogenous matter: a comparison between the Peru upwelling areaand the Sargasso Sea. *Limnol. Oceanogr.* 35 (3), 562–582. doi:10.4319/lo.1990.35.3.0562

Chen, Z., Doering, P. H., Ashton, M., and Orlando, B. A. (2015). Mixing behavior of colored dissolved organic matter and its potential ecological implication in the caloosahatchee river estuary, Florida. *Estuaries Coasts* 38 (5), 1706–1718. doi:10.1007/s12237-014-9916-0

Creed, I. F., Bergström, A.-K., Trick, C. G., Grimm, N. B., Hessen, D. O., Karlsson, J., et al. (2018). Global change-driven effects on dissolved organic matter composition: implications for food webs of northern lakes. *Glob. Change Biol.* 24 (8), 3692–3714. doi:10.1111/gcb.14129

Cullen, J. J., and Davis, R. F. (2003). The blank can make a big difference in oceanographic measurements. *Limnol. Oceanogr. Bull.* 12 (2), 29–35. doi:10.1002/lob.200312229

de Wit, H. A., Valinia, S., Weyhenmeyer, G. A., Futter, M. N., Kortelainen, P., Austnes, K., et al. (2016). Current browning of surface waters will Be further promoted by wetter climate. *Environ. Sci. and Technol. Lett.* 3 (12), 430–435. doi:10.1021/acs.estlett.6b00396

Dempsey, C. M., Brentrup, J. A., Magyan, S., Knoll, L. B., Swain, H. M., Gaiser, E. E., et al. (2020). The relative importance of photodegradation and biodegradation of terrestrially derived dissolved organic carbon across four lakes of differing trophic status. *Biogeosciences* 17 (24), 6327–6340. doi:10.5194/bg-17-6327-2020

Diehl, S., Berger, S. A., Soissons, Q., Giling, D. P., and Stibor, H. (2015). An experimental demonstration of the critical depth principle. *ICES J. Mar. Sci.* 72 (6), 2051–2060. doi:10.1093/icesjms/fsv032

Dittami, S. M., Hostyeva, V., Egge, E. S., Kegel, J. U., Eikrem, W., and Edvardsen, B. (2013). Seasonal dynamics of harmful algae in outer Oslofjorden monitored by microarray, qPCR, and microscopy. *Environ. Sci. Pollut. Res.* 20 (10), 6719–6732. doi:10.1007/s11356-012-1392-0

Dupont, N., and Aksnes, D. L. (2013). Centennial changes in water clarity of the baltic sea and the North Sea. *Estuar. Coast. Shelf Sci.* 131, 282–289. doi:10.1016/j.ecss.2013.08.010

Eiane, K., Aksnes, D. L., and Giske, J. (1997). The significance of optical properties in competition among visual and tactile planktivores: a theoretical study. *Ecol. Model.* 98 (2–3), 123–136. doi:10.1016/S0304-3800(96)01909-6

Elser, J. J., Bracken, M. E. S., Cleland, E. E., Gruner, D. S., Harpole, W. S., Hillebrand, H., et al. (2007). Global analysis of nitrogen and phosphorus limitation of primary producers in freshwater, marine and terrestrial ecosystems. *Ecol. Lett.* 10 (12), 1135–1142. doi:10.1111/j.1461-0248.2007.01113.x

Eriksson, B. K., Johansson, G., and Snoeijs, P. (2002). Long-Term changes in the macroalgal vegetation of the inner gullmar fjord, Swedish Skagerrak Coast1. *J. Phycol.* 38 (2), 284–296. doi:10.1046/j.1529-8817.2002.00170.x

Finstad, A. G., Andersen, T., Larsen, S., Tominaga, K., Blumentrath, S., de Wit, H. A., et al. (2016). From greening to browning: catchment vegetation development and reduced S-deposition promote organic carbon load on decadal time scales in Nordic lakes. *Sci. Rep.* 6 (1), 31944. doi:10.1038/srep31944

Frigstad, H., Andersen, T., Hessen, D. O., Jeansson, E., Skogen, M., Naustvoll, L.-J., et al. (2013). Long-term trends in carbon, nutrients and stoichiometry in Norwegian coastal waters: evidence of a regime shift. *Prog. Oceanogr.* 111, 113–124. doi:10.1016/j.pocean.2013.01.006

Gieskes, W. W. C., Kraay, G. W., and Baars, M. A. (1979). Current 14C methods for measuring primary production: gross underestimates in oceanic waters. *Neth. J. Sea Res.* 13 (1), 58–78. doi:10.1016/0077-7579(79)90033-4

Hansen, J., Sato, M., Ruedy, R., Lo, K., Lea, D. W., and Medina-Elizade, M. (2006). Global temperature change. *Proc. Natl. Acad. Sci.* 103 (39), 14288–14293. doi:10.1073/pnas.0606291103

Heilmann, J. P., Richardson, K., and Ærtebjerg, G. (1994). Annual distribution and activity of phytoplankton in the Skagerrak/Kattegat frontal region. *Mar. Ecol. Prog. Ser.* 112 (3), 213–223. doi:10.3354/meps112213

Howarth, R. W., and Marino, R. (2006). Nitrogen as the limiting nutrient for eutrophication in coastal marine ecosystems: evolving views over three decades. *Limnol. Oceanogr.* 51 (1part2), 364–376. doi:10.4319/lo.2006.51.1_part_2.0364

Johannessen, T., Dahl, E., Falkenhaug, T., and Naustvoll, L. J. (2012). Concurrent recruitment failure in gadoids and changes in the plankton community along the Norwegian Skagerrak coast after 2002. *ICES J. Mar. Sci.* 69 (5), 795–801. doi:10.1093/icesjms/fsr194

Kahle, D., and Wickham, H. (2013). ggmap: spatial Visualization with ggplot2. *R J.* 5 (1), 144. doi:10.32614/RJ-2013-014

Karlsson, J., Byström, P., Ask, J., Ask, P., Persson, L., and Jansson, M. (2009). Light limitation of nutrient-poor lake ecosystems. *Nature* 460 (7254), 506–509. doi:10.1038/nature08179

Kaste, Ø., Gundersen, C. B., Poste, A., Sample, J. E., and Hjermann, D. Ø. (2022). "The Norwegian river monitoring programme 2020 – water quality status and trends," in *72. Norsk institutt for vannforskning*. Available at: https://niva.brage.unit.no/niva-xmlui/handle/11250/2991819.

Kirk, J. T. O. (1994). *Light and photosynthesis in aquatic ecosystems*. Cambridge University Press.

Kolber, Z., Zehr, J., and Falkowski, P. (1988). Effects of growth irradiance and Nnitrogen limitation on photosynthetic energy conversion in Photosystem II 1. *Plant Physiol.* 88 (3), 923–929. doi:10.1104/pp.88.3.923

Kolber, Z., and Falkowski, P. G. (1993). Use of active fluorescence to estimate phytoplankton photosynthesis *in situ*. *Limnol. Oceanogr.* 38 (8), 1646–1665. doi:10.4319/lo.1993.38.8.1646

Kritzberg, E. S., and Ekström, S. M. (2012). Increasing iron concentrations in surface waters - a factor behind brownification? *Biogeosciences* 9 (4), 1465–1478. doi:10.5194/bg-9-1465-2012

Kritzberg, E. S. (2017). Centennial-long trends of lake browning show major effect of afforestation. *Limnol. Oceanogr. Lett.* 2 (4), 105–112. doi:10.1002/lol2.10041

Larsen, S., Andersen, T., and Hessen, D. O. (2011). Climate change predicted to cause severe increase of organic carbon in lakes. *Glob. Change Biol.* 17 (2), 1186–1192. doi:10.1111/j.1365-2486.2010.02257.x

Lawrenz, E., Silsbe, G., Capuzzo, E., Ylöstalo, P., Forster, R. M., Simis, S. G. H., et al. (2013). Predicting the electron requirement for carbon fixation in seas and oceans. *PLoS ONE* 8 (3), e58137. doi:10.1371/journal.pone.0058137

Lundsør, E., Stige, L. C., Sørensen, K., and Edvardsen, B. (2020). Long-term coastal monitoring data show nutrient-driven reduction in chlorophyll. *J. Sea Res.* 164, 101925. doi:10.1016/j.seares.2020.101925

Lundsør, E. (2021). Phytoplankton community dynamics in the Oslofjorden based on a century long time series [Doctoral thesis]. Available at: https://www.duo.uio.no/handle/10852/89509.

Lundsør, E., Eikrem, W., Stige, L. C., Engesmo, A., Stadniczeñko, S. G., and Edvardsen, B. (2022). Changes in phytoplankton community structure over a century in relation to environmental factors. *J. Plankton Res.* 44 (6), 854–871. doi:10.1093/plankt/fbac055

Lyche Solheim, A., Gundersen, H., Mischke, U., Skjelbred, B., Nejstgaard, J. C., Guislain, A. L. N., et al. (2024). Lake browning counteracts cyanobacteria responses to nutrients: evidence from phytoplankton dynamics in large enclosure experiments and comprehensive observational data. *Glob. Change Biol.* 30 (1), e17013. doi:10.1111/gcb.17013

Monteith, D. T., Stoddard, J. L., Evans, C. D., de Wit, H. A., Forsius, M., Høgåsen, T., et al. (2007). Dissolved organic carbon trends resulting from changes in atmospheric deposition chemistry. *Nature* 450 (7169), 537–540. doi:10.1038/nature06316

Morel, A., and Prieur, L. (1977). Analysis of variations in ocean color1. *Limnol. Oceanogr.* 22 (4), 709–722. doi:10.4319/lo.1977.22.4.0709

Nebbioso, A., and Piccolo, A. (2013). Molecular characterization of dissolved organic matter (DOM): a critical review. *Anal. Bioanal. Chem.* 405 (1), 109–124. doi:10.1007/s00216-012-6363-2

Nelson, J. R., and Guarda, S. (1995). Particulate and dissolved spectral absorption on the continental shelf of the southeastern United States. *J. Geophys. Res. Oceans* 100 (C5), 8715–8732. doi:10.1029/95JC00222

Norwegian Centre for Climate Services (NCCS) (2024). Norwegian climate service centre. Available at: https://klimaservicesenter.no/ (Accessed May 15, 2024).

NVE Sildre (2024). Solbergfoss. Available at: https://sildre.nve.no/station/2.605.0 (Accessed September 16, 2024).

Opdal, A. F., Lindemann, C., and Aksnes, D. L. (2019). Centennial decline in North Sea water clarity causes strong delay in phytoplankton bloom timing. *Glob. Change Biol.* 25 (11), 3946–3953. doi:10.1111/gcb.14810

Opdal, A. F., Andersen, T., Hessen, D. O., Lindemann, C., and Aksnes, D. L. (2023). Tracking freshwater browning and coastal water darkening from boreal forests to the Arctic Ocean. *Limnol. Oceanogr. Lett.* 8 (4), 611–619. doi:10.1002/lol2.10320

Opdal, A. F., Lindemann, C., Andersen, T., Hessen, D. O., Fiksen, Ø., and Aksnes, D. L. (2024). Land use change and coastal water darkening drive synchronous dynamics in phytoplankton and fish phenology on centennial timescales. *Glob. Change Biol.* 30 (5), e17308. doi:10.1111/gcb.17308

Opsahl, S., and Benner, R. (1997). Distribution and cycling of terrigenous dissolved organic matter in the ocean. *Nature* 386 (6624), 480–482. doi:10.1038/386480a0

Peterson, B. J. (1980). METHOD: a history of the productivity problem.

Poste, A., Kaste, Ø., Frigstad, H., de Wit, H., Harvey, T., Valestrand, L., et al. (2021). "The impact of the spring 2020 snowmelt floods on physicochemical conditions in three Norwegian river-fjord-coastal systems," in *45. Norsk institutt for vannforskning*. Available at: https://niva.brage.unit.no/niva-xmlui/handle/11250/2829822.

Raval, J. B., Kailasa, S. K., and Mehta, V. N. (2023). "Chapter 3—an overview of optical, physical, biological, and catalytic properties of carbon dots," in *Carbon dots in analytical chemistry*. Editors S. K. Kailasa and C. M. Hussain (Elsevier), 31–41. doi:10.1016/B978-0-323-98350-1.00026-8

Roesler, C., Stramski, D., D'Sa, E., Röttgers, R., and Reynolds, R. A. (2018). Chapter 5: Spectrophotometric Measurements of Particulate Absorption Using Filter Pads. Available at: https://www.researchgate.net/publication/330777169.

Röttgers, R., and Gehnke, S. (2012). Measurement of light absorption by aquatic particles: improvement of the quantitative filter technique by use of an integrating sphere approach. *Appl. Opt.* 51 (9), 1336–1351. doi:10.1364/AO.51.001336

Sætre, R. (2007). *The Norwegian coastal current*. Tapir Academic Press.

Schreiber, U. (2004). Pulse-amplitude-modulation (PAM) fluorometry and saturation pulse method: an overview. *Adv. Photosynth. Respir.* 19, 279–319. doi:10.1007/978-1-4020-3218-9_11

Sejr, M. K., Bruhn, A., Dalsgaard, T., Juul-Pedersen, T., Stedmon, C. A., Blicher, M., et al. (2022). Glacial meltwater determines the balance between autotrophic and heterotrophic processes in a Greenland fjord. *Proc. Natl. Acad. Sci.* 119 (52), e2207024119. doi:10.1073/pnas.2207024119

Smith, R. C., Prezelin, B. B., Bidigare, R. R., and K, S. B. (1989). Bio-optical modeling of photosynthetic production in coastal waters. *Limnol. Oceanogr.* 34 (8), 1524–1544. doi:10.4319/lo.1989.34.8.1524

Spilling, K., Asmala, E., Haavisto, N., Haraguchi, L., Kraft, K., Lehto, A.-M., et al. (2022). Brownification affects phytoplankton community composition but not primary productivity in eutrophic coastal waters: a mesocosm experiment in the Baltic Sea. *Sci. Total Environ.* 841, 156510. doi:10.1016/j.scitotenv.2022.156510

STRÅNG (2024). STRÅNG. Available at: https://strang.smhi.se/ (Accessed January 8, 2024).

Suggett, D. J., Prášil, O., and Borowitzka, M. A. (2010). *Chlorophyll a fluorescence in aquatic sciences: methods and applications* (Netherlands: Springer). doi:10.1007/978-90-481-9268-7

Sverdrup, H. U. (1953). On conditions for the vernal blooming of phytoplankton. *ICES J. Mar. Sci.* 18 (3), 287–295. doi:10.1093/icesjms/18.3.287

Tassan, S., and Ferrari, G. M. (1995). An alternative approach to absorption measurements of aquatic particles retained on filters. *Limnol. Oceanogr.* 40 (8), 1358–1368. doi:10.4319/lo.1995.40.8.1358

Thimijan, R. W., and Heins, R. D. (1983). Photometric, radiometric, and quantum light units of measure: a review of procedures for interconversion. *HortScience* 18 (6), 818–822. doi:10.21273/HORTSCI.18.6.818

Thrane, J.-E., Hessen, D. O., and Andersen, T. (2014). The absorption of light in lakes: negative impact of dissolved organic carbon on primary productivity. *Ecosystems* 17 (6), 1040–1052. doi:10.1007/s10021-014-9776-2

Throndsen, J. (1978). Productivity and abundance of ultra- and nanoplankton in Oslofjorden. *Sarsia* 63 (4), 273–284. doi:10.1080/00364827.1978.10411349

Walday, M., Engesmo, A., Fagerli, C. W., Gitmark, J. K., Gran, S., Kaste, Ø., et al. (2023). Overvåking av ytre Oslofjord 2019-2023—årsrapport 2021.

Wallhead, P., Kristiansen, T., Frigstad, H., Sørensen, K., and Marty, S. (2021). Potential effects of reduced riverine inorganic particle loading on water quality in the Oslofjord region.

Wang, Y.-R., Samset, B. H., Stordal, F., Bryn, A., and Hessen, D. O. (2023). Past and future trends of diurnal temperature range and their correlation with vegetation assessed by MODIS and CMIP6. *Sci. Total Environ.* 904, 166727. doi:10.1016/j.scitotenv.2023.166727

Weyhenmeyer, G. A., Prairie, Y. T., and Tranvik, L. J. (2014). Browning of boreal freshwaters coupled to carbon-iron interactions along the aquatic continuum. *PLOS ONE* 9 (2), e88104. doi:10.1371/journal.pone.0088104

Wit, H. A. de, Stoddard, J. L., Monteith, D. T., Sample, J. E., Austnes, K., Couture, S., et al. (2021). Cleaner air reveals growing influence of climate on dissolved organic carbon trends in northern headwaters. *Environ. Res. Lett.* 16 (10), 104009. doi:10.1088/1748-9326/ac2526

Williamson, C. E., Brentrup, J. A., Zhang, J., Renwick, W. H., Hargreaves, B. R., Knoll, L. B., et al. (2014). Optical metrics as scalable sentinel responses to climate change. *Limnol. Oceanogr.* 59 (3), 840–850. doi:10.4319/lo.2014.59.3.0840

Xiao, Y.-H., Sara-Aho, T., Hartikainen, H., and Vähätalo, A. V. (2013). Contribution of ferric iron to light absorption by chromophoric dissolved organic matter. *Limnol. Oceanogr.* 58 (2), 653–662. doi:10.4319/lo.2013.58.2.0653

Yacobi, Y. (2012). From Tswett to identified flying objects: a concise history of chlorophyll a use for quantification of phytoplankton. *Israel J. Plant Sci.* 60, 243–251. doi:10.1560/IJPS.60.1-2.243